The 3D structure of a periplasm-spanning platform required for assembly of group 1 capsular polysaccharides in *Escherichia coli*

Richard F. Collins*, Konstantinos Beis†, Changjiang Dong†, Catherine H. Botting†, Catherine McDonnell*, Robert C. Ford*, Bradley R. Clarke‡, Chris Whitfield‡§, and James H. Naismith†§

*Faculty of Life Science, University of Manchester, Manchester M60 1QD, United Kingdom; †Centre for Biomolecular Sciences, University of St. Andrews, North Haugh, St. Andrews, Fife KY16 9ST, United Kingdom; and ‡Department of Molecular and Cellular Biology, University of Guelph, Guelph, ON, Canada N1G 2W1

Edited by Susan Gottesman, National Institutes of Health, Bethesda, MD, and approved December 6, 2006 (received for review September 6, 2006)

Capsular polysaccharides (CPSs) are essential virulence determinants of many pathogenic bacteria. *Escherichia coli* group 1 CPSs provide paradigms for widespread surface polysaccharide assembly systems in Gram-negative bacteria. In these systems, complex carbohydrate polymers must be exported across the periplasm and outer membrane to the cell surface. Group 1 CPS export requires oligomers of the outer membrane protein, Wza, for translocation across the outer membrane. Assembly also depends on Wzc, an inner membrane tyrosine autokinase known to regulate export and synthesis of group 1 CPS. Here, we provide a structural view of a complex comprising Wzc and Wza that spans the periplasm, connecting the inner and outer membranes. Examination of transmembrane sections of the complex suggests that the periplasm is compressed at the site of complex formation. An important feature of CPS production is the coupling of steps involved in biosynthesis and export. We propose that the Wza–Wzc complex provides the structural and regulatory core of a larger macromolecular machine. We suggest a mechanism by which CPS may move from the periplasm through the outer membrane.

bacteria | capsule | export | membrane

Escherichia coli isolates produce >80 structurally and immunochemically distinct capsular polysaccharides (CPSs) termed K antigens (1). These polymers vary in monosaccharide composition, glycosidic linkages, and substitution with side-branch glycoses and noncarbohydrate residues. Capsules form a coherent surface layer and are important virulence determinants that typically enable pathogenic bacteria to evade or counteract nonspecific host defenses during the preimmune phase of infection. The two principal biosynthesis pathways for *E. coli* capsules (groups 1 and 2) serve as paradigms for capsule assembly in a broad range of Gram-negative bacteria (2, 3). These include significant pathogens of plants, livestock, and humans (4). The terminal stage in capsule assembly is the translocation of a high-molecular mass (10^5 to 10^6 Da) carbohydrate polymer across the outer membrane. The twin challenges of exporting large polymers from the periplasm to the extracellular space and the coupling of this process to the synthesis of the polymer are common to protein, lipopolysaccharide, and CPS secretion. Almost no structural data exist for any export system involving a periplasmic intermediate. Thus a structural understanding of capsule export not only would provide a platform for the development of new therapeutic strategies but also would illuminate macromolecular secretion in its broader context.

Group 1 capsules are formed by a Wzy-dependent pathway, and many of the early steps in a working model (Fig. 1) have been characterized by direct experimentation or by analogy to conserved processes established in lipopolysaccharide O-antigen synthesis (reviewed in refs. 3–5). In the current model, established by studies with serotype K30, repeat-unit oligosaccharides are assembled on undecaprenol diphosphate lipid carriers at the cytoplasmic face of the inner membrane. These intermediates are then proposed to be transported across the inner membrane into the periplasm by Wzx protein (a flippase). In the periplasm, they then provide substrates for the characteristic Wzy-dependent polymerization process (6). The export of the polysaccharide is mediated by the integral outer membrane lipoprotein, Wza, a member of the outer membrane auxiliary (OMA) family (7), which forms a stable octameric complex (8–10). The export process is coupled to polymerization, because deletion or mutation of Wza does not result in the accumulation of polymer (8, 9). The crystal structure of Wza has recently been determined (11). Wza is best described as a classical amphora without handles. The eight monomers are related by an eightfold axis of rotational symmetry, which runs the length of the amphora. The structure comprises three periplasmic rings that stack one on the other, forming a 100-Å-high barrel structure. The fourth domain is a 40-Å transmembrane α-helical domain formed by the C terminus of the protein. The first ring at the opposite end from the α-helical barrel comprises the conserved polysaccharide export sequence (PES) motif (12). The PES domain has been identified as a common signature in many putative polymer-secreting proteins, but its precise function is unknown.

Two additional proteins are required for both export and polymerization: Wzc, an integral inner membrane tyrosine autokinase, and Wzb, its cognate cytoplasmic phosphotyrosine phosphatase (13–15). The *E. coli* K30 Wzc protein forms a tetramer (16), and each monomer has two predicted transmembrane helices (residues 32–50 and 428–447) that flank a large periplasmic domain (17). The sequence of the periplasmic domain does not match any structurally characterized protein, although its predicted structure is α-helical with coiled-coil motifs (18). The C-terminal cytoplasmic domain of the Wzc protein from serotype K30 contains the tyrosine autokinase activity (13) with seven modifiable tyrosine residues in the last 17 residues. Deletion of the C-terminal region containing these tyrosine residues prevents phosphorylation and halts polymerization and export of high-molecular-weight K30 polysaccharides, although shorter oligosaccharides (one to six repeat units)

Author contributions: C.W. and J.H.N. designed research; R.F.C., K.B., C.D., and B.R.C. performed research; C.D., C.H.B., and C.M. contributed new reagents/analytic tools; R.C.F., C.W., and J.H.N. analyzed data; and C.W. and J.H.N. wrote the paper.

The authors declare no conflict of interest.

This article is a PNAS direct submission.

Freely available online through the PNAS open access option.

Abbreviations: CPS, capsular polysaccharide; PES, polysaccharide export sequence; TEM, transmission EM; OMA, outer membrane auxiliary; CTF, contrast transfer function.

§To whom correspondence may be addressed. E-mail: cwhitfie@uoguelph.ca or naismith@st-and.ac.uk.

This article contains supporting information online at www.pnas.org/cgi/content/full/0607763104/DC1.

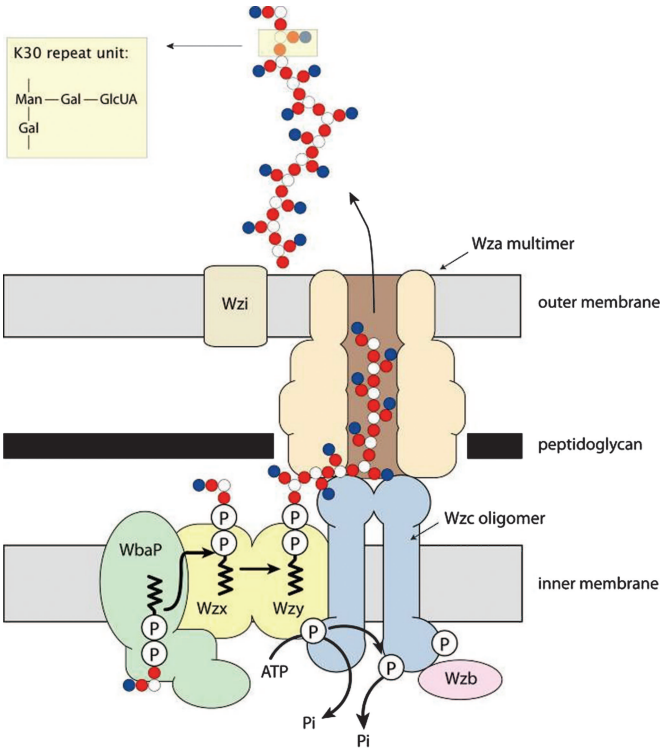

Fig. 1. Schematic view of the interacting proteins required for CPS export. Undecaprenol-PP-linked tetrasaccharide repeat units of serotype K30 capsular polymer are thought to be formed by a sequential process, initiated by the galactose-1-P transferase (WbaP). They are thought to be flipped across the inner membrane by Wzx and are substrates for Wzy-dependent block-wise polymerization. Transphosphorylation of Wzc and its dephosphorylation by Wzb are required to maintain high-level polymerization and capsule export. The outer-membrane lipoprotein, Wza, is essential for export of capsule to the surface, and Wzi is involved in determining the extent of surface attachment of the capsule. For references, see Introduction (reproduced from ref. 11).

can still be formed (13). From the analysis of Wza mutants, it is apparent that the load of tyrosine phosphorylation (rather any specific tyrosine residue) is critical for Wzc function (14). Furthermore, the requirement for the Wzb phosphatase (13) is consistent with a need for cycling of phosphorylation to maintain polymerization and export. This feedback in the CPS export system is evident from the similar acapsular phenotypes of *wza* and *wzc* mutants (13).

Several established lines of evidence have suggested a specific interaction between Wza and Wzc in the bacterial envelope. First, transmission EM (TEM) analysis of the insertion of nascent group 1 CPS on the *E. coli* surface has shown that the sites of insertion are located at regions where the inner and outer membranes are apposed (19–21), consistent with the formation of a transperiplasmic complex. *In vivo* cross-linking of *E. coli* whole cells, with the 12-Å cross-linker dithiobis(succinimidyl-propionate), shows the formation of a large-molecular-weight species involving Wzc and Wza (9). Cross-complementation experiments provide genetic data suggesting molecular recognition between cognate Wza and Wzc pairs (15). Finally, the phenotypes of mutants deficient in Wzc (13) and Wza (8, 9) are consistent with a partnership between Wza and Wzc to maintain feedback control of CPS biosynthesis, although the precise mechanism is unknown. These observations might indicate two roles for Wzc, one involved in interaction with the K30 biosynthesis machinery and the other coupled to the export pathway. However, all available data are consistent with these two critical proteins acting together in coordinating the synthesis of polymer with the subsequent translocation in a putative capsule–assembly complex (Fig. 1). Here we provide definitive evidence for a Wza–Wzc complex and provide the 3D structural characterization of the complex. The complex has significant implications for our understanding of CPS biology.

Results

Structure of the Wza–Wzc Complex. The overexpression, purification, and crystallization of homogeneous Wza lipoprotein have been reported (11, 22). Purified Wzc is heterogeneously phosphorylated, with between zero and three residues in the tyrosine-rich domain phosphorylated [supporting information (SI) Fig. 6]. Because Wzc is purified from native *E. coli* inner membranes, this probably reflects the typical range of the phosphorylation load present in the *in vivo* Wzc population. This is consistent with the finding that no single phosphorylation site is either required or sufficient to allow CPS synthesis and export (14). Purified Wza and Wzc were incubated together, and the mixture was then added to EM grids. The grids were then stained with ammonium molybdate and frozen (*SI Text*). Using a set of 5,945 randomly oriented complex particles, we have determined the 3D structure of the complex using cryonegative staining TEM to ≈12-Å resolution (SI Figs. 7 and 8). Observation of the Wza–Wzc complex by TEM (Fig. 2 *A* and *B*) revealed a homogeneous particle population (SI Fig. 7) with a variety of orientations apparent. The particles were considerably larger than single particles either of Wza (10) (SI Fig. 9) or Wzc (16). Ordered arrays of the complex (Fig. 2*A*) reveal that the complex has a square four-lobed appearance when viewed from the top and displayed a side view reminiscent of an elongated molar tooth. These data indicate that the Wza–Wzc complex results from a highly specific association between the two complexes.

The side view of the complex shows a central cavity in the crown (top of Fig. 2*C*) and four extended roots (bottom of Fig. 2*C*). The long axis (height) is ≈185 Å and runs from the roots to the crown. The width of the complex varies from 100 (edge to edge) to 120 Å (corner to corner) (Fig. 2*C*). The lobed root structures were previously observed in the structure of oligomeric Wzc, whereas the crown has dimensions and appearance corresponding to oligomeric Wza. Furthermore, the complex has evidence for eightfold rotational symmetry in the upper portion of the structure, consistent with Wza crystal structure (11). This changes to a fourfold symmetry in the lower portion of the complex, consistent with tetrameric Wzc (16). Thus, we can assign with confidence the crown as the Wza octamer and the roots as Wzc tetramer (Figs. 2*C* and 3). A 20-Å band in the middle of the structure (Fig. 2*C*) locates the interface between the proteins. The roots of Wzc pass from the periplasm to the cytoplasm, and the crown of Wza corresponds to the three periplasmic rings identified in the crystal structure (11).

Experimental Confirmation of the Topology of the Complex. Several addition experiments were performed to validate the model. The Wza homooligomeric complex was reconstituted into lipid vesicles. Wza hangs from the membrane, with three rings of total width ≈90–100 Å in the aqueous phase (Fig. 4 *A* and *B*), consistent with the crystal structure (11). We previously established that the C terminus of Wza (at the end of the α-helical domain) is exposed on the outer surface of *E. coli* (11). We constructed a Wza variant (Wza-PK) with a PK tag at the C terminus and then formed a heterotrimeric complex (anti-PK Fab, Wza-PK, and Wzc). This complex shows the same cylindrical structure as the Wza–Wzc complex, but it has an additional 40- to 50-Å-wide density located at the end of the complex opposite to Wzc. We attribute this additional density to the Fab fragments bound to the PK epitope at the C terminus of Wza-PK, thus unambiguously locating and orienting Wza within the complex. Immunogold labeling of Wzc-His_6 previously estab-

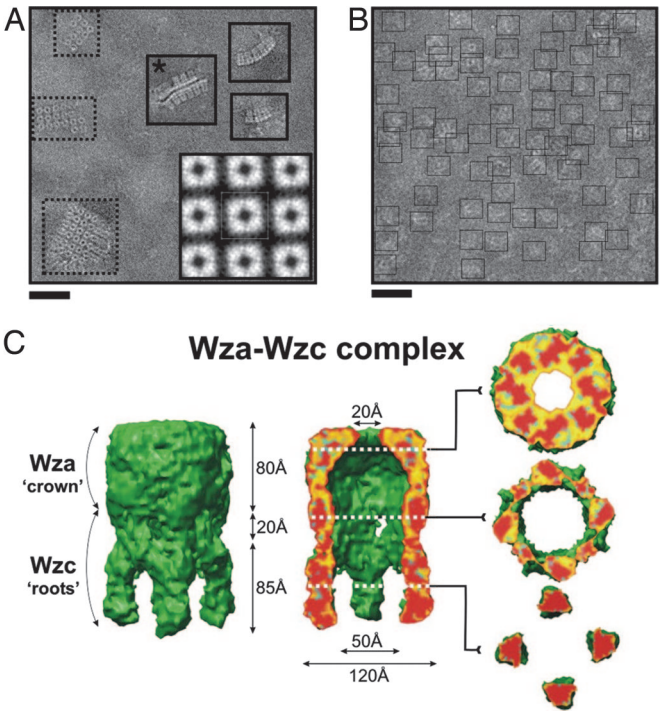

Fig. 2. Electron microscopy and 3D reconstruction of the Wza–Wzc complex. (*A*) 1D and 2D arrays of Wza–Wzc complexes. A cryonegatively stained field displaying a variety of ordered crystals of the Wza–Wzc complex. Side views presenting 1D arrays (solid boxes) and *p*4 2D crystal top views (dotted boxes) formed spontaneously in solution at a low frequency. Occasionally side-view arrays adopted a D-symmetrical arrangement (*), indicating the complex is an asymmetric structure and self-interacts, most likely by intercalating the cone-shaped α-helical domains of the Wza portion of the complex. Images have been CTF-corrected and contrast-enhanced for presentation. (Scale bar, 500 Å.) The *p*4 projection map (*Inset Right*) was calculated by merging 10 small 2D crystal areas (each containing 10–25 individual top-view complexes) in CRISP following lattice unbending (40). Unit cell: $a = 110$ Å, $b = 110$ Å, $\gamma = 90°$. (*B*) TEM of Wza–Wzc complexes. Shown are individual reconstituted Wza–Wzc complexes cryonegatively stained and recorded under cryo conditions described in SI Table 1. Individual complexes are in multiple orientations relative to the carbon support film (highlighted in boxes). Images have been CTF-corrected and contrast-enhanced for presentation. (Scale bar, 500 Å.) (*C*) 3D structure of the Wza–Wzc complex. The C4 symmetrized 3D map of the Wza–Wzc complex (*Left*) is displayed by using surface rendering at a threshold (1.1 σ above the mean density) appropriate to accommodate 800 kDa of mass (≈320-kDa Wza and 320-kDa Wzc proteins and ≈160 kDa of detergent). Fifty percent of the foremost volume (*Center*) is removed to reveal the internal structure and overall dimensions of the central cavity and the pore. Detail through the height of the complex is revealed in the slices (*Right*), displayed at the intervals indicated by the dotted lines, and parallel to the rotational long axis. Density thresholds of 2 σ (yellow), 3 σ (turquoise), and 3.5 σ (red) are used in the slices.

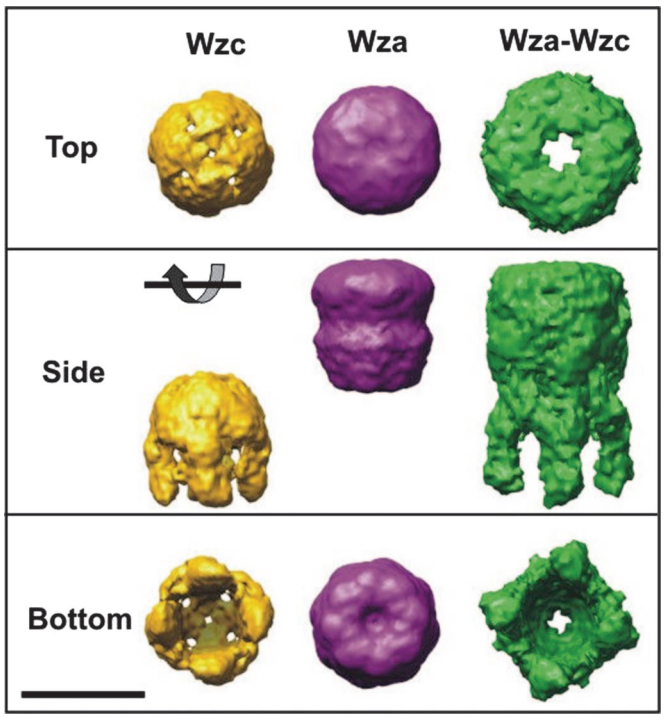

Fig. 3. Comparison of the Wza–Wzc complex with TEM structures of oligomeric Wza and Wzc. The Wzc protein and the Wza–Wzc complexes are displayed with C4 symmetry applied and are displayed at thresholds appropriate to accommodate ≈400 kDa (320-kDa protein and 80-kDa detergent) and ≈800 kDa (640-kDa protein and 160-kDa detergent) of mass, respectively. In light of the recently published crystal structure (11), the Wza structure presented here is recalculated in C8 symmetry from the original EM data set (10), as described in *Discussion*. The surface is displayed a threshold appropriate to accommodate ≈400-kDa mass (320-kDa protein and 80-kDa detergent). Structures are filtered to resolutions of 16 Å (individual Wza and Wzc proteins) and 12 Å (Wza–Wzc complex). (Scale bar, 100 Å.)

lished the periplasmic and cytoplasmic portions of this integral inner membrane protein complex (16). A comparison of the EM structure of Wza alone and in the Wza–Wzc complex with the Wza x-ray structure (Figs. 3 and 5) reveals that the transmembrane α-helical nozzle is not resolved in EM structures.

Discussion

EM Structure of Wza. The unprecedented features of the Wza crystal structure (11) prompted us to reevaluate the cryonegatively stained EM structure of the Wza octamer (10). Both structural studies identified Wza as an octamer with a large internal cavity, and the dimensions of the EM structure match the three periplasmic rings seen in the crystal structure. Although the broad features of the EM model were correct, the EM approach did not resolve the α-helical transmembrane region. Four- rather than eightfold symmetry was applied in the original analysis because of the distinctive square profiles of some particle classes. Moreover, the circular mask used in the original analysis, in retrospect, was too small to comfortably accommodate the longest dimension of Wza. This would have exacerbated a mixing of side with top views and probably accounts for the clipping of its periplasmic and extracellular extremities. Reanalysis with a larger mask using the crystal structure as a starting model generated a much more consistent structure. Using a threshold level set by the volume of the crystal structure, the side portals seen before (10) are no longer apparent. However, they are evident if an artificially high threshold value is applied. With the increased mask diameter, the three-banded arrangement of the Wza periplasmic domain is clear; however, the C-terminal α-helical domain is still not seen. Our failure to observe the α-helical domain in either Wza or the Wza–Wzc complex could be due to ammonium molybdate preferentially interacting with the α-helical domain, eliminating contrast. Alternatively, the helical domain may be disordered under the negative-staining conditions used for the isolated Wza or the Wza–Wzc complex. In the presence of the lipid bilayers, the α-helical domain of isolated Wza is apparently inserted into the membrane bilayer with no significant change in the remaining periplasmic structure. This provides experimental support for the predicted transmembrane α-helical barrel (11) and suggests our failure to visualize the α-helical domain is not the result of some large artifactual change in Wza structure.

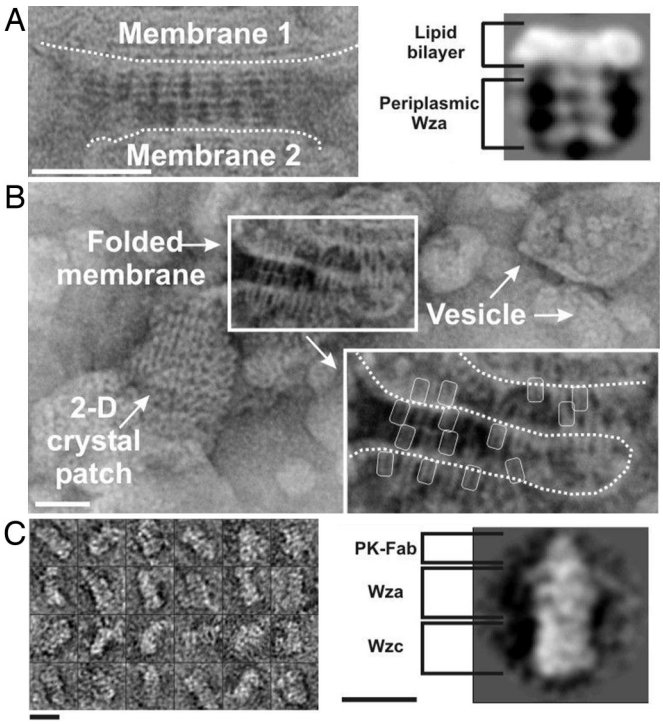

Fig. 4. Reconstitution of Wza into membranes and localization of its C terminus in the Wza–Wzc complex. (*A*) Wza inserts into membranes with an asymmetric distribution of mass. EM of negatively stained Wza oligomers reconstituted into dioleoylphosphatidylcholine vesicles. (Scale bar, 500 Å.) Wza oligomers reconstituted into two separate vesicles are revealed, effectively forming intercalated contacts between them. The lipid bilayers are indicated by the dotted lines. The projection map (*Right*) shows the average (37) of the seven complexes (protruding downward from membrane 1 and upward from membrane 2) and has been low-pass-filtered to 20 Å. (Scale bar, 100 Å.) (*B*) Different types of Wza interaction within lipid vesicles. One area of the image shows a 2D crystal patch. Side views illustrate a membrane that is folded, and the magnified *Inset* shows intercalated Wza with a selection of particles boxed. The location of the membrane is shown by the dotted line, and boxes indicate some of the Wza oligomers. (Scale bar, 500 Å.) (*C*) EM of the (Wza-PK)-Wzc complex labeled with PK-Fab. The montage shows a selection of individual (Wza-PK)–Wzc complexes incubated with PK Fab. Data were CTF-corrected and contrast-enhanced for presentation but have not undergone any alignment procedure. Selection box. 260 Å^2. The projection map shows the class average from 48 such views [EMAN (37)] low-pass-filtered to 30-Å resolution. (Scale bar, 100 Å.)

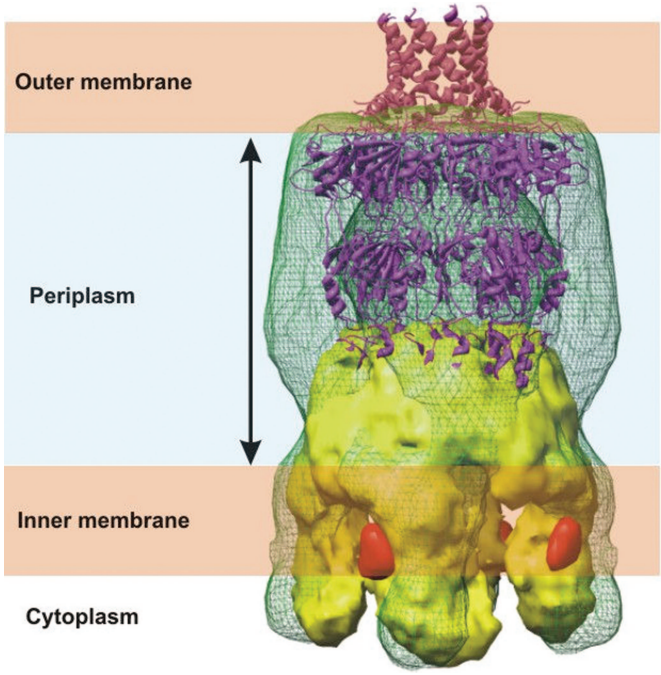

Fig. 5. Proposed organization of Wza–Wzc in the bacterial outer envelope. The 3D structure of Wza–Wzc is shown in green wire frame (at the same display threshold as in Figs. 2*B* and 4). The Wza x-ray structure (11) (purple ribbon) and Wzc (yellow) have been fitted manually into the complex volume using CHIMERA. The orange densities indicate the previously calculated position of Ni-NTA gold labels bound to the N terminus of Wzc (16). The inferred locations of the inner and outer membrane bilayers are shown relative to the Wza–Wzc complex. The structure of the complex suggests that Wza undergoes major conformations in the region encompassing the PES domain, which interacts with Wzc. The EM envelope suggests that Wza has increased its width in response to the opening of the PES domain.

Mechanistic Implications of the Wza–Wzc Complex. In the Wza–Wzc complex, the periplasmic domain of Wza interacts with the periplasmic domain of Wzc. The proven interaction of Wza with Wzc *in vivo* (9), the homogenous nature of the complex particles on EM grids (SI Fig. 7), the observation of 2D crystals of the complex (Fig. 2*A*), and the correspondence with the crystal structure of Wza (Figs. 3 and 5) all argue that the complex we observe is not an unanticipated *in vitro* artifact. Although the α-helical domain of Wza is not seen, the epitope tag at the C terminus of Wza-PK binds Fab fragments without significantly changing the structure (Fig. 4*C*). The precise interface between Wza and Wzc cannot be identified, because it appears there is significant conformation change in both proteins during complex formation. In the complex, the Wza oligomer has opened out to form a pore of 22-Å diameter (Figs. 2*C* and 3) that leads into the large central cavity from the periplasm. This is a profound change, because the central cavity is closed to the periplasm in both the EM (10) and x-ray structure of Wza (11). The closed nature of isolated Wza presumably ensures the integrity of the permeability barrier of the cell envelope, which prevents access of large (potentially harmful) molecules into the cell or loss of critical periplasmic components.

Fitting the crystal structure of Wza into the EM data indicates that the region encompassing the PES domain of Wza interacts with Wzc. Moreover, it is the PES domain that has apparently undergone a significant conformational change. It is important to note that some OMA proteins do not interact with a Wzc homolog; the group 2 capsule system of *E. coli* does not include Wzc (3). However, a functional role in gating a channel formed by an OMA family member would explain the conservation of the PES domain in the OMA superfamily (11). The envelope of the EM structure suggests that, as a result of the opening of the PES domain, Wza increases in width relative to the isolated protein. We propose that the CPS enters the central cavity of Wza through the newly opened PES domain. From this central cavity, it then exits from the periplasm and passes to the extracellular space through the α-helical domain of Wza. The association with Wzc apparently triggers this active or open conformation of Wza, and the data therefore offer one feasible structural explanation for the role of Wzc in regulating export. Although the roots of Wzc pass through the cytoplasmic membrane, Wzc does not create a channel; the gaps between the roots would be filled by the lipid bilayer. The cytoplasmic disk of protein found in isolated Wzc has apparently separated in the complex and forms spurs at the top of each root (Figs. 2*C* and 3). The precise point of entry of the polymer from the periplasmic polymerization site into the central cavity is unclear; it seems most likely that it enters Wza through the newly opened PES domain. The complex does have small holes on the side that could potentially serve as access points for the nascent polymer

from the periplasm. Although the conformation changes are attractive with respect to our model for polymer export, we cannot entirely discount the possibility that these changes result from cryonegative staining. However, the individual components were also stained, thus minimizing artifacts in the complex relative to its components.

Implications of the Wza–Wzc Complex for Structure of the Gram-Negative Cell Envelope. The Wza–Wzc complex provides a powerful insight into the interactions of the CPS export machinery. Using x-ray crystallographic data, we can now assign with confidence the relative position of Wza and Wzc within the complex (Fig. 5) and hence the juxtaposition of the inner and outer membranes. We have established, through a combination of Ni-NTA-nanogold labeling of cytoplasmic N-terminal hexahistidine tagged isolated Wzc and modeling of an homologous ATP-binding domain, that the legs of Wzc were located in the cytoplasm (16) (Fig. 5). The location of the gold label allowed us to position the inner membrane in the Wza–Wzc complex with reasonable confidence limits ±10 Å (16). These considerations imply that ≈30 Å (±10 Å) (i.e., the length of one Wzc leg) is located in the cytoplasm, consistent with the mass of cytoplasmic tyrosine kinase domain of Wzc. These conservative assumptions imply a maximum width of the periplasmic region of Wzc of between 25 and 45 Å. The crystal structure of Wza (11) and calculations from the EM images of the Wza–Wzc complex inserted in the lipid bilayer (Figs. 4*A* and 5) establish that there is a 100-Å-long protein structure suspended into the periplasm from the inner leaflet of the outer membrane. This leaves a periplasmic region of 145 Å at most and potentially as small as 125 Å. The width of the periplasm accessible to solutes will be further reduced by at least 20 Å due to the polar head groups of the lipid leaflets flanking the periplasm. A solute-accessible periplasmic thickness of ≈145 Å or less (Fig. 5) is narrower than the 200 Å measured in electron micrographs of frozen thin sections (23). However, it is close to the ≈150 Å estimated from the structural model of the needle complex for type III protein secretion (24).

Implications of the Wza–Wzc Complex for CPS Export. The Wza–Wzc complex provides compelling experimental evidence that the inner (cytoplasmic) and outer membranes are linked at the site of polymer export. The existence of regions where the two membranes come into close apposition was observed in cryo-EM work on thin-sectioned *E. coli* bacteria (20). Points of membrane adhesion were found both as isolated sites and extended arrays (20) and were predicted to be important in macromolecular export (20, 23). Notably, some of these domains were found to coincide with the sites of attachment of group 1 capsule-specific bacteriophages to their polymeric receptor on the cell surface, after activation of polymer synthesis in conditional mutants (19, 21). This local compression of the periplasm would serve as a site for recruitment of other machinery required for polymer export. For example, the spurs formed by Wzc could serve as a focal point for further protein–protein interactions in a complex mediating coordinated synthesis and export of CPS. Large protein assemblies, in effect molecular machines, are an increasingly common motif in cell biology. The targeting of other export complexes to the site of periplasm compression would lead to extended stretches of cytoplasmic and outer membrane contact and could serve to localize CPS export within the cell.

Relevance to Other Secretion Processes. There are important parallels and differences between our observations for the Wza–Wzc complex and the processes occurring in bacterial protein secretion (reviewed in ref. 25). The only other such complete secretion complex to be visualized directly is the needle complex involved in type III secretion (24). The needle complex forms a channel through the outer and inner membranes (24), allowing proteins from the cytoplasm to exit the cell, bypassing the periplasm. The evolutionarily related flagellar basal body also spans the periplasm (26–28). A periplasm-spanning AcrAB-TolC drug efflux complex is thought to exist in *E. coli* (29–34), although the complete complex itself has not been visualized. Typically, in other secretion systems, additional adaptor proteins either bridge the gap between inner and outer membrane proteins or are required for complex formation (25, 33, 35, 36). In contrast, the Wza–Wzc complex exports material from the periplasm and links the inner to outer membrane without the apparent need for additional proteins. No comparable structural data exist for Type II and IV protein secretion systems; however, both act on distinct periplasmic intermediates (25) and involve multiple proteins. Our data establish that a membrane-spanning complex is at the heart of CPS export and provide a framework for analyzing other systems for macromolecular export in Gram-negative bacteria.

Materials and Methods

Wza and Wzc Purification. The expression, extraction, and purification of native Wza (22) and N-terminally His-tagged Wzc (9, 10, 16) have been reported. Protein integrity was confirmed by gel electrophoresis before EM.

Mass Spectrometry of Wzc. Wzc protein was resolved by SDS/PAGE and visualized by staining with Coomassie brilliant blue. The Wzc band was excised and subjected to in-gel digestion. Gel sections were destained by washing with acetonitrile and subjected to reduction and alkylation before digestion with trypsin at 37°C. Peptides were then extracted with 10% formic acid and analyzed by MALDI-TOF mass spectrometry by using a Micromass TofSpec 2E instrument (Micromass, Manchester, U.K.). The sample (0.5 μl) was target-spotted with 0.5 μl of α-cyano-4-hydroxycinnamic acid. Data were calibrated by using the tryptic peptides of β-gal (Sigma, St. Louis, MO) and lock-mass-corrected by using a Glu-Fibrinopeptide B spike. Wzc fragments were also analyzed by nanoliquid chromatography electrospray ionization tandem MS, and data for doubly and triply charged precursor ions were converted to centroid data (without smoothing) by using the Mascot Daemon 2.1 (Matrix Science, London, U.K.) data import filter for Sciex Analyst (Toronto, ON, Canada).

Formation of a Specific Wza–Wzc Complex. Ten microliters of Wza and 10 μl of Wzc [both at 700 μg /ml in 25 mM Tris, pH 7.5/80 mM NaCl/0.008%(wt/vol) *n*-dodecyl-D-maltoside] were mixed together and left at 4°C for 18 h. Samples were centrifuged for 5 min at 30,000 × *g* before preparation for cryonegative staining, as described below.

EM Preparation. Carbon-coated copper grids (no. 400) were glow-discharged and placed shiny side down on the surface of a 5-μl droplet of the Wza–Wzc mixture for 2 min and then immediately placed on a 20-μl droplet of freshly prepared 12% (wt/vol) ammonium molybdate (pH 6.8) and 1% (wt/vol) trehalose for several seconds. Grids were then briefly blotted onto double-layered Whatman (Brentford, U.K.) 50 filter paper. Data were recorded by using a CM200 FEG electron microscope with an Oxford (Oxford, U.K.) system cryostage at ≈100 K. Images were recorded at defocus values of 2–2.5 μm and were processed as previously described.

Image Processing. The 3D structure of the Wza–Wzc complex, with Wzc present in the variably phosphorylated state (SI Fig. 6) was calculated by using EMAN (37). Additional processing data used for structure calculation are shown in SI Table 1. The complete data set of 5,945 complex particles was interactively

selected by using BOXER (37) and contrast normalized. The contrast transfer function (CTF) for each particle in the data set was determined by using the program CTFIT (37), and corrections for amplitudes and phases were applied by using a GroEL structure factor data set kindly provided by S. Ludtke (Baylor College of Medicine, Houston, TX).

3D Structure Calculation. As a first step, reference-free class averages were generated with the complex orientated in multiple particle positions. By following previously described strategies (10, 16, 38–40), a preliminary 3D model was determined from single-particle averaging classes that represented distinct views of the Wza complex. Although there is an inherent symmetry mismatch (Wza is octameric, whereas Wzc is tetrameric), the symmetries are harmonic, and it is best practice to apply the lowest common symmetry in such cases; C4 symmetry was applied. The relative orientations of the characteristic views were determined by using a Fourier common-lines routine, and the resulting averages were combined to generate the preliminary 3D model. The 3D structure was subsequently refined by using eight rounds of iterative projection matching. Each refinement was assessed by examining convergence with the Fourier Shell Correlation (FSC) of the 3D models. The final 3D volume fully converged after six rounds of iterative refinement. Resolution was determined to be ≈12 Å by using the FSC = 0.5 criterion described (40) (SI Fig. 8). To test that the convergence procedure did not depend on any initial model bias, refinement was tested by using separate models. Start models of a rectangular cylinder or an elliptical density of appropriate dimensions both produced essentially equivalent structures.

Reconstitution of Wza into Lipid Bilayers. Two milligrams of dioleoylphosphatidylcholine was dissolved in 100 μl of chloroform/ethanol (1:1$_{vol/vol}$), then dried under N_2. The lipid film was further dried under vacuum for 1.5 h and dissolved in 50 μl of 25% octyl-glucoside (β-OG) with reconstitution buffer (20 mM Tris/80 mM NaCl/0.15 mM $MgCl_2$, pH 7.5) to result in a final lipid concentration of 2 mg/ml DOPC in 1.25% β-OG (wt/vol). Wza was reconstituted at a protein concentration of 0.2 mg/ml (overall lipid:protein ratio of 5:1). Ten BioBeads (Bio-Rad, Hercules, CA) were equilibrated in buffer and added before incubating the mixture for 16 h at 4°C with agitation to remove detergent. Before examination by EM, samples were mixed briefly on a vortex mixer, decanted, and applied to EM grids. The grids were negatively stained by using 4% uranyl acetate, as described (10, 17).

PK-Fab Labeling of Wza. The paramyxovirus SV5 PK tag was added to the C terminus of Wza to make Wza-PK. The residues were added by the PCR by using the forward primer AGGAGGAATTCATGAAGAAAAAACTTGTTAGATTTTCGCATGCTGCAGTTA**GGTGGAGTCCAATCCCAGCAAAGGGTTTGGGATCGGCTTTCC**GTTGGGCCATCTCTTAATGTATC.

The addition of the tag was confirmed by DNA sequencing and the integrity of the tag by Western blotting using the PK monoclonal antibody as primary antibody [mouse; kindly provided by R. Randall (University of St. Andrews)] and second antibody (anti-mouse), as described (41) (SI Fig. 10). Expression of Wza-PK was carried out with the same conditions used to produce protein for crystallization (24). Controls included cells grown under conditions inducing WT Wza (Wt-Wza) expression and cells containing Wza-PK but grown under noninducing conditions (i.e., no arabinose). The cells were directly visualized with a Delta Vision restoration microscope (SI Fig. 10) and confirmed the C-terminal tag in Wza-PK was extracellular. For experiments with Wza–Wzc complexes involving Wza-PK, 0.5 mg/ml PK-Fab (25 mM Tris, pH 7.5) was incubated with 2 mg/ml PK-tagged Wza–Wzc complex [25 mM Tris, pH 7.5/80 mM NaCl/0.008% (wt/vol) *n*-dodecyl-D-maltoside] for 2 h at 4°C. The PK-Fab-labeled complex was then imaged in the same manner as the Wza–Wzc complex.

Immunofluorescence microscopy of cells was carried out by Margaret Taylor. We thank Dr. Peiyi Wang at the University of Sheffield (Sheffield, U.K.) for cryo-EM technical support. We are grateful to the reviewers for constructive comments that have significantly improved the manuscript. J.H.N. is a career development Fellow of the Biotechnology and Biological Science Research Council (U.K.) (Biotechnology and Biological Sciences Research Council). C.W. holds a Canada Research Chair. This work is supported by a program grant from the Wellcome Trust (to J.H.N.) and by Canadian Institutes of Health Research (C.W.).

1. Jann K, Jann B (1997) in *Escherichia coli: Mechanisms of Virulence*, ed Sussman M (Cambridge Univ Press, Cambridge, UK), pp 113–143.
2. Whitfield C, Roberts IS (1999) *Mol Microbiol* 31:1307–1319.
3. Whitfield C (2006) *Annu Rev Biochem* 75:39–68.
4. Whitfield C, Paiment A (2003) *Carbohydr Res* 338:2491–2502.
5. Raetz CRH, Whitfield C (2002) *Annu Rev Biochem* 71:635–700.
6. Drummelsmith J, Whitfield C (1999) *Mol Microbiol* 31:1321–1332.
7. Paulsen IT, Park JH, Choi PS, Saier MH (1997) *Fems Microbiol Lett* 156:1–8.
8. Drummelsmith J, Whitfield C (2000) *EMBO J* 19:57–66.
9. Nesper J, Hill CM, Paiment A, Harauz G, Beis K, Naismith JH, Whitfield C (2003) *J Biol Chem* 278:49763–49772.
10. Beis K, Collins RF, Ford RC, Kamis AB, Whitfield C, Naismith JH (2004) *J Biol Chem* 279:28227–28232.
11. Dong CJ, Beis K, Clarke BR, Brunkan A, Whitfield C, Naismith JH (2006) *Nature* 444:226–230.
12. Bateman A, Birney E, Cerruti L, Durbin R, Etwiller L, Eddy SR, Griffiths-Jones S, Howe KL, Marshall M, Sonnhammer ELL (2002) *Nucleic Acids Res* 30:276–280.
13. Wugeditsch T, Paiment A, Hocking J, Drummelsmith J, Forrester C, Whitfield C (2001) *J Biol Chem* 276:2361–2371.
14. Paiment A, Hocking J, Whitfield C (2002) *J Bacteriol* 184:6437–6447.
15. Reid AN, Whitfield C (2005) *J Bacteriol* 187:5470–5481.
16. Collins RF, Beis K, Clarke BR, Ford RC, Hulley M, Naismith JH, Whitfield C (2006) *J Biol Chem* 281:2144–2150.
17. Doublet P, Grangeasse C, Obadia B, Vaganay E, Cozzone AJ (2002) *J Biol Chem* 277:37339–37348.
18. Morona R, Van Den Bosch L, Daniels C (2000) *Microbiol* 146:1–4.
19. Bayer ME, Thurow H (1977) *J Bacteriol* 130:911–936.
20. Bayer ME (1991) *J Struct Biol* 107:268–280.
21. Bayer ME (1979) in *Bacterial Outer Membranes: Biogenesis and Functions*, ed Inouye M (Wiley, New York), pp 167–202.
22. Beis K, Nesper J, Whitfield C, Naismith JH (2004) *Acta Crystallogr D* 60:558–560.
23. Matias VRF, Al-Amoudi A, Dubochet J, Beveridge TJ (2003) *J Bacteriol* 185:6112–6118.
24. Marlovits TC, Kubori T, Sukhan A, Thomas DR, Galan JE, Unger VM (2004) *Science* 306:1040–1042.
25. Kostakioti M, Newman CL, Thanassi DG, Stathopoulos C (2005) *J Bacteriol* 187:4306–4314.
26. Francis N, Thomas D, Sosinsky G, Derosier D (1995) *Mol Biol Cell* 6:687–687.
27. Francis NR, Sosinsky GE, Thomas D, Derosier DJ (1994) *J Mol Biol* 235:1261–1270.
28. Thomas D, Francis N, Sosinsky G, Derosier D (1992) *FASEB J* 6:A29–A29.
29. Nikaido H, Zgurskaya HI (2001) *J Mol Microbiol Biotechnol* 3:215–218.
30. Holland IB, Blight MA (1999) *J Mol Biol* 293:381–399.
31. Andersen C, Hughes C, Koronakis V (2000) *EMBO Rep* 1:313–318.
32. Andersen C, Hughes C, Koronakis V (2001) *Curr Opin Cell Biol* 13:412–416.
33. Thanabalu T, Koronakis E, Hughes C, Koronakis V (1998) *EMBO J* 17:6487–6496.
34. Koronakis V, Eswaran J, Hughes C (2004) *Annu Rev Biochem* 73:467–489.
35. Letoffe S, Delepelaire P, Wandersman C (1996) *EMBO J* 15:5804–5811.
36. Balakrishnan L, Hughes C, Koronakis V (2001) *J Mol Biol* 313:501–510.
37. Ludtke SJ, Baldwin PR, Chiu W (1999) *J Struct Biol* 128:82–97.
38. Collins RF, Davidsen L, Derrick JP, Ford RC, Tonjum T (2001) *J Bacteriol* 183:3825–3832.
39. Collins RF, Ford RC, Kitmitto A, Olsen R, Tonjum T, Derrick JP (2003) *J Bacteriol* 183:3825–3832.
40. Collins RF, Frye SA, Kitmitto A, Ford RC, Tonjum T, Derrick JP (2004) *J Biol Chem* 279:39750–39756.
41. Hanke T, Szawlowski P, Randall RE (1992) *J Gen Virol* 73:653–660.